



Cite this: *New J. Chem.*, 2021, 45, 19889

One-pot preparation of multicomponent photocatalyst with (Zn, Co, Ni)(O, S)/Ga₂O₃ nanocomposites to significantly enhance hydrogen production†

Hairus Abdullah, ^a Riski Titian Ginting,^b Anita Christine Sembiring,^a Noto Susanto Gultom, ^c Hardy Shuwanto ^c and Dong-Hau Kuo^{*c}

To enhance the production of hydrogen as an alternative energy to fossil fuel, multicomponent photocatalyst (Zn, Co, Ni)(O, S)/Ga₂O₃ nanocomposites were synthesized and optimized with different amounts of Ga precursor in a relatively low-temperature process. The as-prepared nanocomposites were characterized by XRD, SEM, TEM, XPS, DRS, PL, EIS, TPC, CV, and MS techniques, and tested for their photocatalytic activities toward hydrogen evolution reactions (HERs). Zn(O, S) phase formation with low amounts of Ni and Co dopants and a Ga₂O₃ secondary phase were confirmed. The HER catalytic activity of the as-prepared nanocomposite could achieve ~9 mmol g⁻¹ h⁻¹ without any noble metal as a cocatalyst under low-power UV-light-illuminated conditions. Ethanol was used as the hole scavenger to enhance the photocarrier separation during the photocatalytic HER. It was found that Ni–Co codopants played an essential role in improving HER activities of Zn(O, S). Although the wide-bandgap Ga₂O₃ is not active for photoexcitation under 365 nm light irradiation, it is believed that oxygen vacancies in Ga₂O₃ induce the electron transfer from the conduction band of (Zn, Ni, Co)(O, S). This charge transfer contributes to the photocarrier separation, leading to a higher photocatalytic activity. Moreover, based on XPS results, the trivalent Ni dopant also generated positively charged antisite defects, which also helps electron trapping, reducing the electron–hole recombination rate. This work demonstrated a nanomaterial-design strategy involving simultaneously using dopants and nanocomposite concepts to enhance hydrogen production with an aim to solve the global energy issue.

Received 17th June 2021,
Accepted 29th September 2021

DOI: 10.1039/d1nj02980k

rsc.li/njc

1. Introduction

As the utilization of energy for human life increases every year, fossil fuel consumption has been inevitably escalated and has induced the global warming effect on the earth. To reduce the use of fossil fuels, many efforts to find alternative sustainable energy sources, such as hydrogen as an energy carrier, have been made.^{1–6} The hydrogen-based energy source with its relatively higher combustion energy compared to fossil fuels is a preferred energy source due to its clean combustion product in the environment. However, most hydrogen production is classically obtained from the petroleum and natural gas steam

reforming process.⁷ This method is not sustainable for long-term application since the actual source of hydrogen is also derived from fossil fuel. To replace this practice of hydrogen production, the use of an advanced photocatalytic hydrogen evolution reaction (HER) is preferred due to its more simple processing.^{8–10} However, the works on HER need high efficiency for actual applications together with a minimum reverse effect on our environment. Therefore, HER photocatalysts with the characteristics of low cost, low light-power input, abundance of the chemicals in nature, high efficiency, environmental safety, good reusability, and possible sunlight harvesting are required.

To advance the works on HER, some strategies, such as the use of metal cation^{11–15} or non-metal anion doping,^{16,17} nanocomposite with and without a p-n heterojunction,^{13,18–24} utilizing metal–organic framework materials,²⁵ oxygen vacancies,^{26–28} hole scavengers,^{29,30} and introducing a cocatalyst in to the catalytic system,^{31–34} have been explored toward achieving a better HER efficiency. In addition, some works have also utilized plasmonic materials, such as Ag, Au, and Pt, to enhance the localized surface

^a Department of Industrial Engineering, Universitas Prima Indonesia, Medan, Indonesia. E-mail: hairus@unprimdn.ac.id

^b Department of Electrical Engineering, Universitas Prima Indonesia, Medan, Indonesia

^c Department of Materials Science and Engineering, National Taiwan University of Science and Technology, No. 43, Section 4, Keelung Road, Taipei 10607, Taiwan. E-mail: dhkuo@mail.ntust.edu.tw

† Electronic supplementary information (ESI) available. See DOI: 10.1039/d1nj02980k

electrons during the photoreaction, leading to a higher charge transfer and lower recombination of photocarriers.^{35–39} In these works, hydrogen reduction requires a material with a more negative conduction band (CB) than the reduction potential of hydrogen;⁴⁰ therefore, an electron will be easily transferred from CB to reduce the absorbed proton on the catalyst surface to form hydrogen gas.

To fulfill the required band-structure positions for HER, semiconductors with a negative CB, such as ZnO and ZnS, are viewed as promising candidates in developing the water-splitting process.^{41,42} Rao *et al.* successfully fabricated ZnS@NiO nanostructure to enhance the hydrogen production rate to 1.6 mmol g^{−1} h^{−1} under sunlight illumination.⁴³ Zhao *et al.* designed a material system comprising CeO₂/g-C₃N₄ with a Z-scheme heterojunction for the degradation of bisphenol A and for HER.⁴⁴ Zhang *et al.* also reported the p-type NiSe₂/n-type Cd_{0.5}Zn_{0.5}S for efficient charge separation to produce hydrogen.⁴⁵ Yang *et al.* utilized CdS with NiV LDH nanosheets to form a p–n heterojunction for efficient hydrogen generation.⁴⁶ In order to harness the full visible-light spectrum from solar light, Xu *et al.* engineered 2D-hBN/g-C₃N₄ with a Z-scheme heterojunction for metal-free photocatalytic hydrogen evolution.⁴⁷ Furthermore, to utilize π -conjugated carbon for its better adsorption property, Dao *et al.* wrapped N-doped CeO₂ with N-doped graphene to improve the visible-light HER. The nitrogen doping here acted as a plasmonic material to enhance the charge transfer during the photoreactions.⁴⁸ In other progress, Yamakata *et al.* attempted to dope Zn simultaneously with Ca on β -Ga₂O₃ photocatalysts for water splitting. The Zn and Ca created shallow mid-gap states and enhanced electron trapping to prevent electron–hole recombination.⁴⁹ In these works, all the single-phase materials did not exhibit remarkable catalytic performance, implying electron and hole recombination was lower with multi-phase materials.^{50,51}

Among the dopant materials are Ni and Co transition metals, which can induce different surface defects on a catalyst. They can considerably enhance the charge separation and lower the charge-transfer resistivity, leading to higher catalytic activities.^{7,52,53} Further investigations by Bai *et al.* also indicated that NiCo-oxy-sulfide nanocages exhibited high efficiency in generating hydrogen.⁵⁴ In addition, the Ni and Co-based materials are also suitable for supercapacitor and battery applications,^{55–57} which is related to their impressive charge transfer and storage properties. Moreover, Ga₂O₃ also provides a suitable energy band position for the water-splitting process.^{49,58} Therefore, it would be interesting to simultaneously use Ni and Co dopants to design a photocatalyst system with another secondary phase for better photocarrier separation, as indicated by other works.^{37,59}

In this work, a Zn-oxy-sulfide catalyst was simultaneously modified with Ni and Co dopants and composited with a Ga₂O₃ phase for enhanced HER. Here, the second phase Ga₂O₃, which forms a heterojunction composite, helps hamper the recombination between holes and electrons after photoexcitation.⁶⁰ The catalytic system was investigated with constant amounts of 10% Ni and 2.5% Co dopants by varying the content of Ga₂O₃.

A number of our previous works studied the use of a single dopant of Ni or Co.^{10,52,61} It was expected that the additional secondary phase Ga₂O₃ would induce a better photocarrier separation, leading to a higher reaction efficiency. Here, it was demonstrated that a suitable amount of Ga₂O₃ addition to the catalyst system significantly enhanced the photocatalytic HER activity by up to 50%. The HER mechanism reactions on the catalyst system were elucidated and are described herein.

2. Experimental

2.1. Materials

All the chemicals used in this work were commercially obtained. Zinc acetate dihydrate with a purity of 98% was purchased from Alfa Aesar. Cobalt(II) nitrate hexahydrate ($\geq 98\%$), nickel(II) chloride (98%), and gallium(III) nitrate hydrate (99.9%) were kindly provided by Sigma-Aldrich. Hydrazine monohydrate (99%) was purchased from Acros Organic. Ethanol with a purity of 95% was supplied by Jingmei Chemical Company. The chemicals were directly used without any purification treatment.

2.2. Synthesis of (Zn, Co, Ni)(O, S)/Ga₂O₃ nanocomposites

The synthesis process was done based on the previous procedure.⁶² In this work, the molar amounts of Zn, Ni, and Co were kept constant with variation of the Ga amount to obtain different composite powders. The Ni and Co molar amounts were, respectively, 10% and 2.5% based on the molar amount of Zn precursor. In a typical preparation, 20 mmol Zn(Ac)₂·2H₂O, 2 mmol NiCl₂, 0.5 mmol Co(NO₃)₃·6H₂O, 10 mmol thioacetamide (TAA), and different molar amounts of 0%, 2.5%, 5%, 10%, and 20% Ga(NO₃)₃·8H₂O were dissolved in 500 mL deionized (DI) water in separate glass beakers. The percentages of Ga precursors were calculated based on the amount of Zn precursor. The process was done under vigorous stirring with an elevated temperature at 95 °C for 4 h. During the heating process, 0.5 mL hydrazine monohydrate was dropped into the reaction solution after 95 °C was reached. A white precipitate was obtained after 4 h reaction and was collected by centrifugation. The precipitate was washed three times with ethanol and dried at 80 °C overnight. The obtained powders with different amounts of 0%, 2.5%, 5%, 10%, and 20% Ga precursor were denoted as ZNC-0G, ZNC-2.5G, ZNC-5G, ZNC-10G, and ZNC-20G, respectively.

2.3. Characterization

Field-emission scanning electron microscopy (FESEM, JSM 6500F, JEOL, Tokyo, Japan) was used to examine the morphology and microstructure, together with energy dispersive spectroscopy (EDS), and elemental mapping analysis of the as-prepared catalysts. The crystal structures of the catalyst powders were identified by the X-ray diffraction (XRD) patterns recorded on a Bruker D2-phaser diffractometer using Cu K α radiation with a wavelength of 1.5418 Å. High-resolution images and the selected area electron diffraction patterns of the catalyst particles were observed with field-emission gun transmission electron microscopy (FEG-TEM,

Philips Tecnai F30, USA). The specific surface area, pore size, and pore volume were analyzed using the Brunauer–Emmett–Teller (BET) method with nitrogen adsorption–desorption isotherms. Nitrogen adsorption and desorption were isothermally done at 77.15 K with a constant-volume adsorption apparatus utilizing a Novatouch LX2 Quantachrome Instrument (Boyton Beach, FL, USA). Optical absorbances of the catalyst powders were analyzed with diffuse reflectance spectroscopy (DRS) and photoluminescence (PL) using a Jasco V-670 UV-visible-near IR spectrophotometer. The charge transfer and electrochemical properties of the catalysts were analyzed by electrochemical impedance spectroscopy (EIS), transient photocurrent (TPC), cyclic voltammetry (CV), and Mott–Schottky (MS) measurements with a Bio-Logic Science Instrument supported by EC-Lab software. To conduct the three-electrode electrochemical measurements during the analysis, a glassy carbon electrode (GCE), Ag/AgCl/sat KCl, and platinum plate were used as the working, reference, and counter electrodes, respectively. The chemical states of the elements and their contents in the as-prepared catalysts were examined by X-ray photoelectron spectroscopy (XPS) carried out on a VG ESCA Scientific Theta Probe spectroscope with Al K α (1486.6 eV). The confirmation of the generated hydrogen was done by gas chromatography (GC-1000) with a thermal conductivity detector (TCD). A molecular-sieve (MS-5A 60/80; 3.5 m \times 1/8") column was utilized in the GC measurement to separate the gases during the photocatalytic reactions.

2.4. Photocatalytic hydrogen evolution experiments

Photocatalytic HER was done in a 500 mL homemade reactor with a tubular space in the middle of the reactor for inserting a 352 nm UV lamp as the light source for the photoreactions. The reactor was also equipped with input and output channels for the carrier gas. During the photocatalytic experiments, 225 mg catalyst powder was dispersed in 450 mL solution with 10% v/v alcohol as a hole scavenger reagent. A UV-blacklight lamp (4 \times 6 W) was used as the light source for the catalytic reaction. As only two-thirds of the lamp was inserted into the reactor, the illumination power was less than 24 W. Before starting the light illumination, the catalyst-dispersed solution was purged with 99% Ar for 1 h to remove atmospheric gases in the reactor under vigorous magnetic stirring. After removing all the atmospheric gases and ensuring no contaminants were present in the reactor by GC analysis, the photocatalytic HER was started by turning on the light source. Gas sampling was performed every 30 min by flowing Ar gas from the reactor to the GC to monitor the evolved hydrogen gas from the photoreaction. A similar measurement procedure was done for the as-prepared catalysts with different Ga₂O₃ contents.

3. Results and discussion

3.1. X-ray diffraction (XRD) pattern analysis

The crystal structures of the ZNC-0G, ZNC-2.5G, ZNC-5G, ZNC-10G, and ZNC-20G catalysts were identified by XRD pattern analysis. Fig. 1 indicates the XRD patterns of the nanocomposite

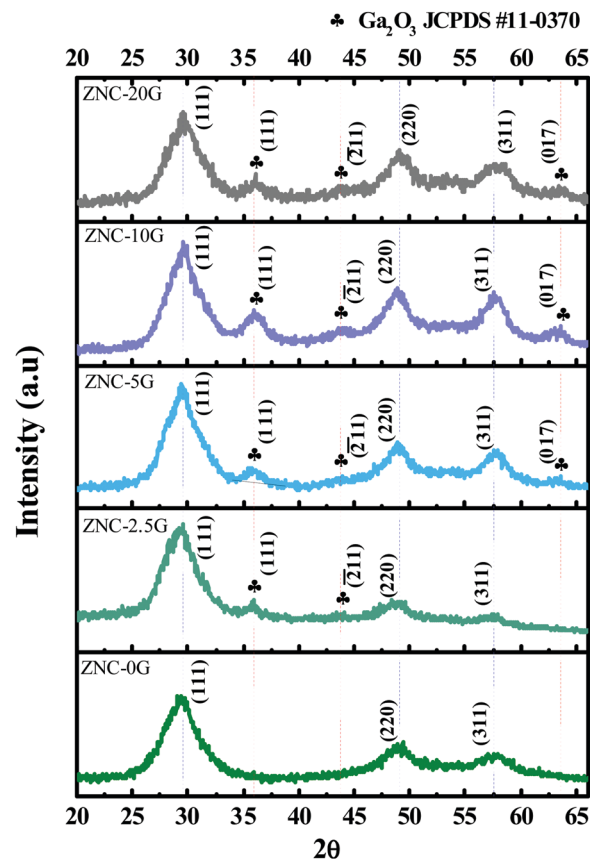


Fig. 1 XRD patterns of the as-prepared catalyst powders with different contents of Ga₂O₃.

catalysts with different Ga₂O₃ amounts, as mentioned in the experimental procedure. ZNC-0G without a Ga content exhibited a sphalerite Zn(O, S) pattern, consistent with the previous work.⁶³ The peaks at (111), (220), and (311) in the ZNC-0G pattern corresponded to the oxysulfide phase located between those of cubic ZnO (JCPDS #65-2880) and ZnS (JCPDS #05-0566). However, the incorporation of Ni and Co into ZNC-0G did not show a noticeable peak shift since the atomic radii of Ni and Co are about the same as Zn.⁶⁴ A secondary phase of Ga₂O₃ was confirmed with the peaks at (111), ($\bar{2}11$), and (017), which gradually appeared at high contents of Ga precursor. The overall XRD patterns confirmed the Ni-Co-doped Zn(O, S) formation with an additional Ga₂O₃ phase. Based upon the XRD results, the as-prepared ZNC-xG (x = 2.5, 5, 10, and 20) catalysts were confirmed as Ni-Co-doped Zn(O, S)/Ga₂O₃ nanocomposites through the two patterns that existed in the XRD analysis. Based on the Scherrer calculation at the (111) peak, the crystalline sizes of Ni-Co-doped Zn(O, S) and Ga₂O₃ were found to be 2.5 and 5.2 nm, respectively.

3.2. Morphology and microstructure of the ZNC-xG (x = 2.5, 5, 10, and 20) nanocomposites

The morphology and microstructures of the ZNC-xG catalyst powders were further examined by SEM analysis. Fig. 2 indicates the SEM images of the as-prepared ZNC-xG (x = 2.5, 5, 10, and 20) nanocomposites. The particle size of the

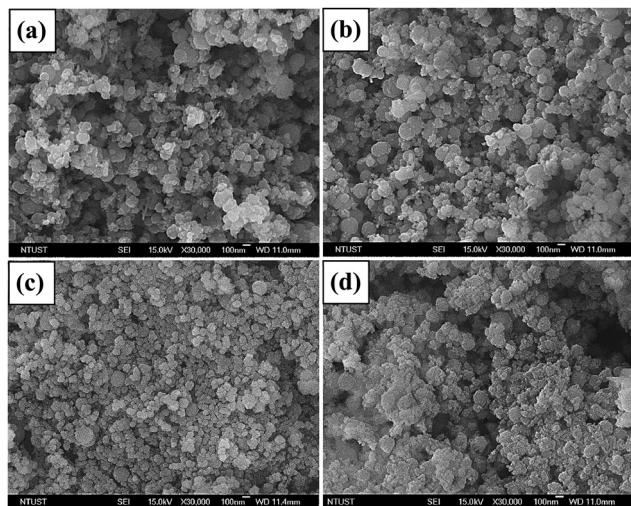


Fig. 2 SEM images of the (a) ZNC-2.5G, (b) ZNC-5G, (c) ZNC-10G, and (d) ZNC-20G catalyst powders.

nanocomposites approximately ranged from 50 to 250 nm. There were no obvious differences in their morphology. However, the catalyst powder with $x = 10$ for ZNC-10G exhibited a relatively uniform particle size (about 100 nm) in its microstructure. This might be due to the appropriate amounts of Ni, Co, and Ga during the preparation process.

Further analysis was done by elemental mapping to show all the existing elements in the microstructure. Fig. 3 shows the elemental mapping of ZNC-10G with different pixel contrast colors for the Zn, Ni, Co, Ga, O, and S elements. The elemental contrasts revealed the major phase of the catalyst was Zn(O, S) with minor amounts of Ni and Co dopants. The Ga amount in Ga_2O_3 was also relatively low. However, the amounts of O and S were comparable, as indicated by their similar contrasts in the elemental mapping. The related EDS analysis is also provided in Table S1 in the ESI.†

In addition, the morphology of ZNC-10G was also identified by transmission electron microscopy through the high-resolution image, lattice fringes, and electron diffraction pattern. Fig. 4a shows the high-resolution image with a particle size of about 100 nm, consistent with the SEM analysis. As confirmed with the Scherrer calculation, the tiny particle size was naturally aggregated to form a bigger particle with an average size of 100 nm. Fig. 4b indicates the lattice fringes in the area shown with a red square in Fig. 4a. The lattice fringes of Zn(O, S) were found at 2.72, 2.73, 3.10 Å, which are consistent with a previous study.² Several lattice fringes were noticed since the formation of a solid solution between ZnO and ZnS induces a variation in the oxysulfide composition on its surfaces. The observed lattice parameters (d -spacings), which were located between those of ZnO and ZnS at (111), were confirmed with the edges of a broad ring pattern in the SAED analysis (see Fig. 4c). Therefore, the order was $d_{\text{ZnO}} < d_{\text{Ni-Co-doped Zn(O,S)}} < d_{\text{ZnS}}$ at (111) as indicated with the yellow solid-line circles for ZnO and ZnS in Fig. 4c. The lattice fringe of Ga_2O_3 (2.54 Å) was also noticeable at (111) and supported with a low-intensity ring pattern, as shown with the red dashed-line

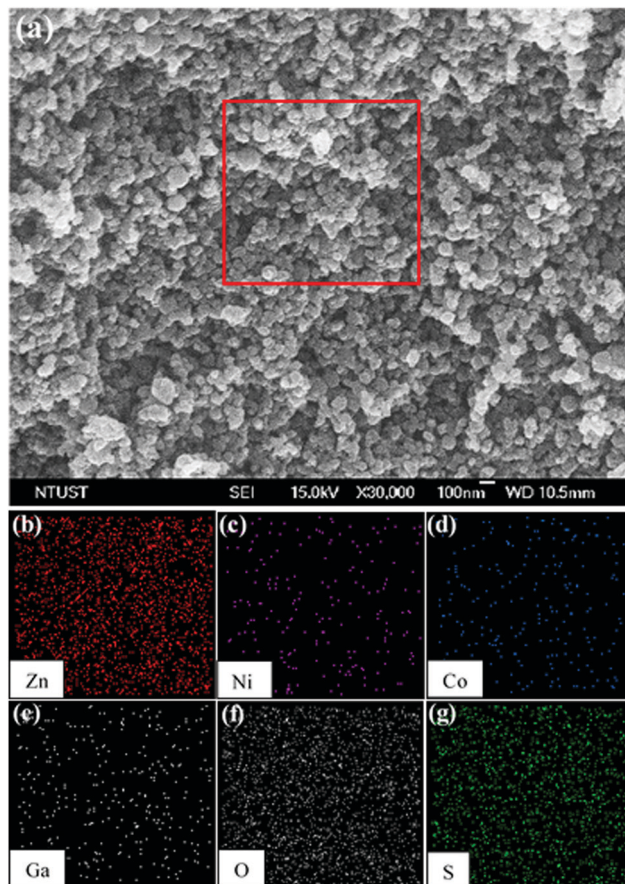


Fig. 3 Elemental mapping of the ZNC-10G catalyst powder to indicate the existing elements by color contrast.

circle in Fig. 4c. The SAED analysis confirmed the primary phase of Zn(O, S) with a minor Ga_2O_3 phase after doping with Ni and Co, which is consistent with the XRD analysis.

3.3. Diffuse reflectance spectra (DRS) and photoluminescence (PL) analyses

The optical properties of ZNC- x G ($x = 0, 2.5, 5, 10$, and 20) catalysts were probed with diffuse reflectance spectroscopy and photoluminescence analyses. The DRS spectra were analyzed from 250–600 nm to obtain the UV and vis absorbances of the catalysts, as shown in Fig. 5a. All of the catalysts possessed relatively high UV and low visible-light absorbances due to the wide bandgap, as indicated by the Tauc plots in Fig. 5b. The bandgap energy of the as-prepared nanocomposite was noticed mainly around 3.57–3.59 eV. The major contribution to the bandgap energy was from the Zn(O, S) phase with Co and Ni dopants. As the Ga_2O_3 phase was relatively low, the slope of Ga_2O_3 was not noticeable in the Tauc plot. Based on the DRS analysis, a blacklight UV-tube lamp with an emission wavelength of 365 nm was applied as a light source in this work.

The crucial property of a photocatalyst is its ability to separate the photogenerated electrons and holes during the photoreaction. Redox reactions on catalyst surfaces would be successfully done if the photocarriers could diffuse to the

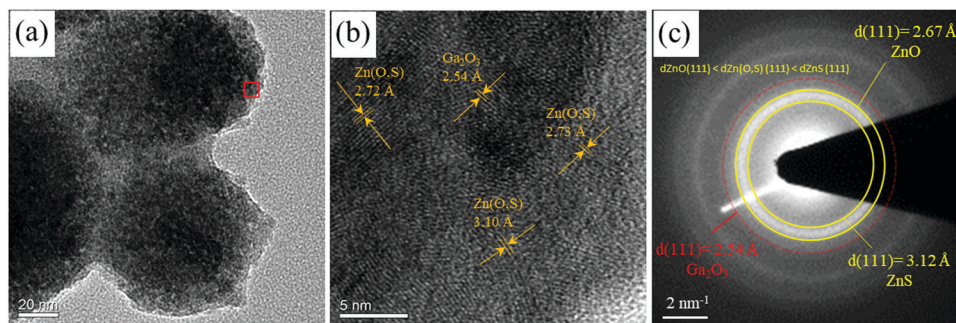


Fig. 4 (a) High-resolution TEM image, (b) lattice fringes, and (c) selected area electron diffraction (SAED) ring pattern of the ZNC-10G catalyst.

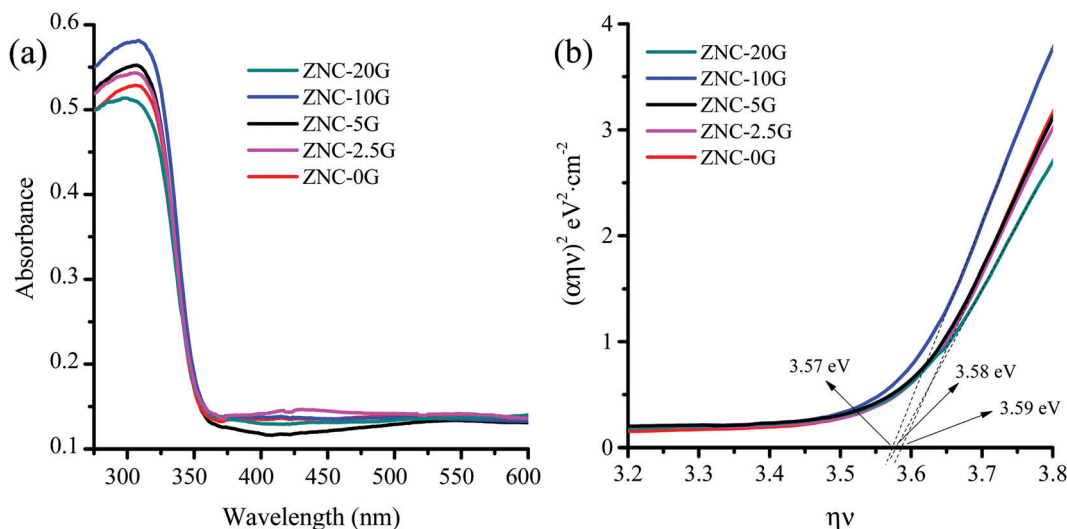


Fig. 5 (a) Diffuse reflectance spectra and (b) Tauc plots of ZNC-xG ($x = 0, 2.5, 5, 10$, and 20) catalysts.

interfaces of the catalyst and solution without undergoing the recombination process. If the lifetime of the photocarriers is sufficiently long for a photoreaction, the catalytic activities could be enhanced. To probe the capability of the ZNC-xG ($x = 0, 2.5, 5, 10$, and 20) catalysts for separating the photocarriers and to evaluate the recombination process, PL measurements were applied. Fig. 6 shows the PL spectra of the ZNC-xG ($x = 0, 2.5, 5, 10$, and 20) catalysts with a 250 nm excitation wavelength. The observation of the photoemission during the PL measurement was done from 300–700 nm. Based on the DRS and Tauc plot analysis, the prominent peak of PL might be around 350 nm. However, the PL spectra exhibited a prominent peak at 410 nm and some other minor peaks at 470 and 500 nm, indicating defects or trapping states in the conduction or valence bands due to the Ni and Co dopants.⁶⁵ Some defect states at 430–550 nm might be related to oxygen vacancy defects in the lattice.⁶⁶ A curve with a lower intensity in the PL spectra indicates a lower recombination rate between photoexcited electrons and holes. The ZNC-10G catalyst showed a relatively low photoemission intensity in the range of 350–410 nm, implying a relatively lower recombination rate in the catalyst. Based on the PL result, ZNC-10G might exhibit excellent photocatalytic activity for the HER process.

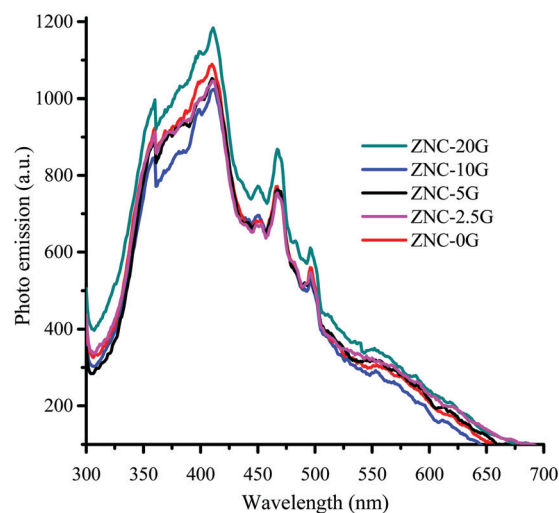


Fig. 6 Photoluminescence spectra of ZNC-xG ($x = 0, 2.5, 5, 10$, and 20) catalysts with a 250 nm excitation wavelength.

3.4. X-ray photoelectron spectroscopy (XPS) analysis

To understand the chemical states and composition of the nanocomposite, ZNC-10G was selected for XPS analysis. XPS

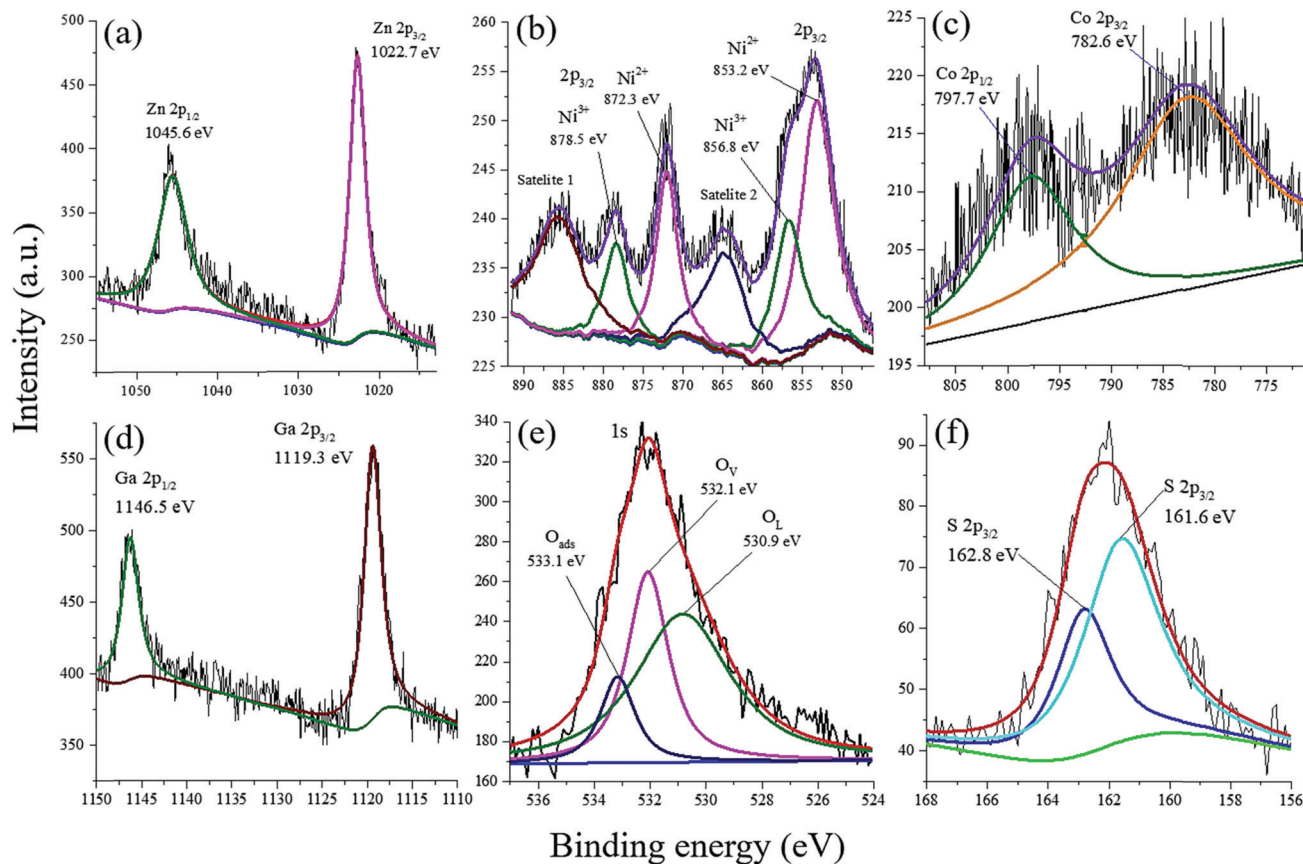


Fig. 7 High-resolution XPS spectra of (a) Zn 2p, (b) Ni 2p, (c) Co 2p, (d) Ga 2p, (e) O 1s, and (f) S 2p orbitals in the ZNC-10G nanocomposite.

measurement is a powerful spectroscopic technique to characterize the surface chemical states of materials. Fig. 7 indicates the high-resolution spectra of the Zn 2p, Ni 2p, Co 2p, Ga 2p, O 1s, and S 2p orbitals in the ZNC-10G nanocomposite. The binding energy of the Zn $2p_{3/2}$ and $2p_{1/2}$ orbitals were, respectively, indicated at 1022.7 and 1045.6 eV in Fig. 7a, predicting the state of Zn^{2+} , which is consistent with the previous works.^{9,10,62} The spectra of the Ni dopant with Ni^{2+} and Ni^{3+} were also found, as shown in Fig. 7b, with their satellite peaks. The binding energies of Ni^{2+} $2p_{3/2}$ and $2p_{1/2}$ orbitals were revealed at 853.2 and 872.3 eV, respectively. Consistently, the states of the Ni^{3+} $2p_{3/2}$ and $2p_{1/2}$ orbitals were also noticed at 856.8 and 878.5 eV, respectively.⁶⁷ Fig. 7c indicates the relatively low-intensity peaks of the Co $2p_{3/2}$ and $2p_{1/2}$ orbitals at 782.6 and 797.7 eV, respectively, thus confirming the low amounts of Co^{2+} in the nanocomposite. These results well agreed with the previous work.⁶¹ Furthermore, Ga $2p_{3/2}$ and $2p_{1/2}$ orbitals could be observed at 1119.3 and 1146.5 eV, respectively, in Fig. 7d.⁶⁸ Fig. 7e confirms the states of oxygen in the nanocomposite were oxygen in the lattice (O_L), oxygen vacancy (O_V), and adsorbed oxygen (O_{ads}), coming from the hydroxide group. Also, O_L , O_V , and O_{ads} were noticed at 530.9, 532.1, and 533.1 eV, respectively, after the peak deconvolution from the O 1s orbital.¹⁰ Based on the area of O 1s peak, the ratios of O_L , O_V , and O_{ads} were 56%, 32%, and 12%, respectively. The oxygen vacancy might be contributed from the vacancy sites on

Zn(O, S) and Ga_2O_3 . A positive oxygen vacancy state is essential for electron trapping, leading to photocarrier separation during photoreaction.^{62,69} As the formation of defects in the crystal will occur after incorporating Ni and Co into Zn(O, S) lattice, some antisite defects of Ni_{Zn}^{0+} , Ni_{Zn}^{+} , and Co_{Zn}^{0+} also will be formed to compensate for the mass, charge, and energy balance. The positive Ni_{Zn}^{+} can help to trap electrons and enhance the catalytic activity. Moreover, the different dopants in the lattice will induce the lattice strain energy, enhancing chemical adsorption on the catalyst surfaces.⁷⁰ Finally, the chemical state of S 2p orbital was also confirmed in Fig. 7f. The binding energies at 161.6 and 162.8 eV corresponded to S $2p_{3/2}$ and $2p_{1/2}$ orbitals, respectively.⁵⁹

In addition, the elemental composition based on the area of high-resolution peaks was calculated and the results are shown in Table 1. The elemental analysis revealed ZNC-10G mainly consisted of Zn(O, S) with 1% Ni and 0.8% Co dopants. The secondary phase of Ga_2O_3 contained only 2.4% Ga. The cation-to-anion ratio was calculated to be 0.95, indicating oxygen

Table 1 XPS compositional analysis of the ZNC-10G nanocomposite

Elements in the ZNC-10G nanocomposite								
Zn	Ni		Co	Ga	O			S
	Ni^{2+}	Ni^{3+}			O_L	O_V	O_{ads}	
36.1%	0.6%	0.4%	0.8%	2.4%	20.2%	11.3%	4.3%	23.9%

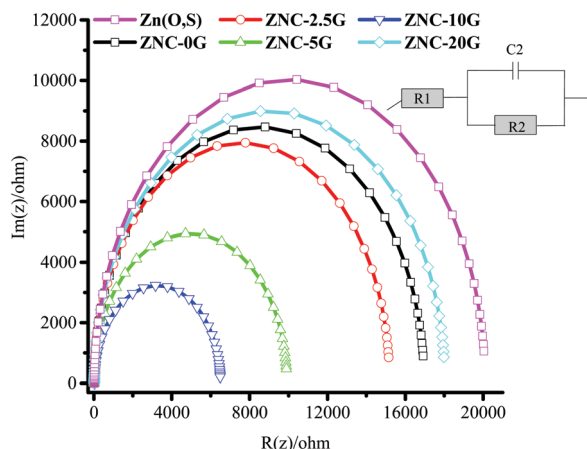


Fig. 8 EIS spectra of ZNC-xG ($x = 0, 2.5, 5, 10$, and 20) with different Ga_2O_3 contents.

vacancies with positive charge will compensate for the unbalanced ratio. Consequently, 11.3% V_O appeared in the analysis, which was required to balance the charge from the defects in the lattice. The indication of an oxygen vacancy was also found in the PL analysis. Furthermore, 4.3% O_ads species were also found, indicating that the chemisorbed oxygen played an essential role in stabilizing the surface charge. The XPS results were consistent with the XRD, TEM, and PL analyses, confirming the $(\text{Zn}, \text{Ni}, \text{Co})(\text{O}, \text{S})$ and Ga_2O_3 phases in the ZNC-10G nanocomposite.

3.5. Electrochemical impedance spectroscopy (EIS) measurements

EIS analysis is an essential method to probe the resistivity of charge transfer during the catalytic reaction on an electrode surface. The EIS data are generated by applying an alternating current to the electrode, then measuring the response, and recording the phase shift and amplitude changes over a range of applied frequencies.⁷¹ A perturbative characteristic of the electrochemical process is described in the Nyquist plot to obtain the charge-transfer resistance of a catalytic cell.⁸ Fig. 8 presents the Nyquist plots of different ZNC-xG catalyst systems. A smaller semicircle curve implies a lower resistivity of charge transfer on the working electrode. Here, with the increasing amounts of Ga_2O_3 content, the resistivity of the catalyst decreased. ZNC-10G exhibited a minor semicircle diameter compared to the others. The EIS spectra were fitted with the Randles electrical circuit, as shown in the inset Fig. 8, to obtain the charge-transfer resistance. The resistivity of ZNC-0G decreased from 16 949 Ω to 15 139, 9850, and 6503 Ω for ZNC-2.5G, ZNC-5G, and ZNC-10G, respectively. In addition, the resistivity of $\text{Zn}(\text{O}, \text{S})$ without doping exhibited the highest value (~ 20 K Ω) among the other catalyst systems. However, after incorporating Ga_2O_3 into the Ni-Co-doped $\text{Zn}(\text{O}, \text{S})$, the conductivity was enhanced $\sim 62\%$ compared to the pristine Ni-Co-doped $\text{Zn}(\text{O}, \text{S})$ and $\text{Zn}(\text{O}, \text{S})$. This enhanced conductivity might be contributed to by the oxygen vacancy in Ga_2O_3 , as confirmed by the XPS analysis. It was supposed that ZNC-10G

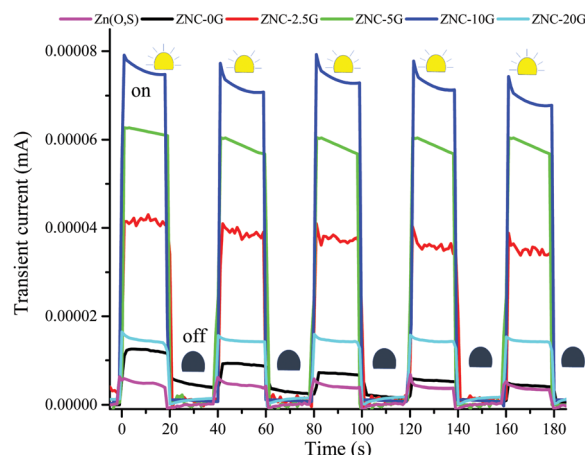


Fig. 9 Transient photocurrent of ZNC-xG catalysts with different Ga contents in the light-on and -off conditions.

with the lowest charge-transfer resistance would possibly induce a high catalytic activity.

3.6. Photoresponse measurement

Photoresponse measurements of ZNC-xG were done to examine the ability of the catalysts to generate photocarriers in on/off-light illuminated conditions with a frequency of 25 mHz. A UV LED light was used as a light source in this measurement. A three-electrode system was also applied to the measurement with a catalyst-fixed glassy carbon electrode (GCE), Pt plate, and $\text{Ag}/\text{AgCl}/\text{KCl}$ electrode as the working, counter, and working electrodes, respectively. Fig. 9 indicates the transient photocurrent of the different ZNC-xG catalysts under light-on and -off conditions. The data showed that ZNC-xG for $x = 0, 2.5, 5, 10$, and 20 exhibited currents of 12.5, 42.5, 62.0, 76.0, and 14.7 μA , respectively. Furthermore, the photoresponse of pristine $\text{Zn}(\text{O}, \text{S})$ was also low compared to the others due to its highest resistivity. The transient photocurrents indicated ZNC-10G might facilitate a great photocatalytic reaction, supported by the excellent optical absorbance in the DRS analysis, lowest emission in PL analysis, and lowest resistivity of charge transfer in the EIS analysis.

3.7. Cyclic voltammetry (CV) analysis

To probe the stability of ZNC-10G in conducting reduction and oxidation reactions, cyclic voltammetric measurements were done in 0.1 M KCl solution with 5 mM $\text{K}_3[\text{Fe}(\text{CN})_6]$ and $\text{K}_4[\text{Fe}(\text{CN})_6]$ as a redox couple reagent. ZNC-10G was well dispersed into Nafion solution and deposited on a 1 cm^2 carbon cloth (CC) for use as a working electrode. $\text{Ag}/\text{AgCl}/\text{saturated KCl}$ and Pt plate were used as the reference and counter electrodes, respectively. Fig. 10 shows the CV spectra of the ZNC-10G catalyst for 100 cycles of reduction and oxidation. The cathodic and anodic peaks were related to the reduction and oxidation of Fe^{3+} and Fe^{2+} , respectively, and were noted at 0.12 and 0.35 V in the CV spectra. The cathodic and anodic currents were observed at -0.17 and $1.8 \mu\text{A cm}^{-2}$, respectively, implying the oxidation capability might be higher than the reduction capability of the catalyst. As the oxidation and reduction

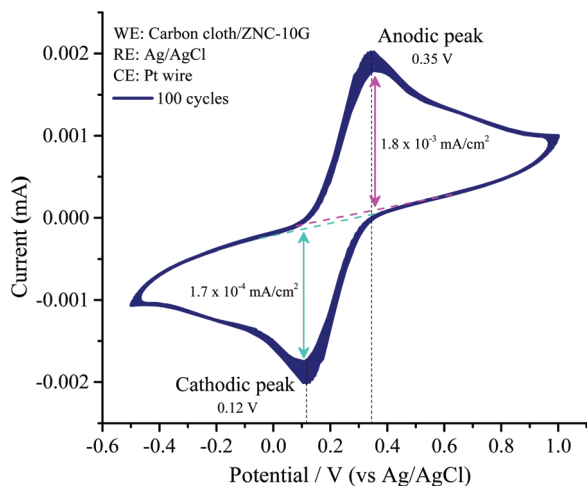


Fig. 10 Cyclic voltammogram of the ZNC-10G catalyst in 0.1 M KCl solution containing a redox couple reagent with 5 mM $K_3[Fe(CN)_6]$ and $K_4[Fe(CN)_6]$.

peaks were not significantly decreased after 100 cycle redox reactions, the ZNC-10G catalyst was considered as relatively stable and possessed potential for a long-term application. To prove the stability of the photocatalytic reaction, ZNC-10G was recycled and used for the catalytic reaction repeatedly for 5 cycles, as shown in Fig. S1 (ESI[†]). It was noticed that the photocatalytic HER performance still reached 90% after five cycles of the reusability experiment.

3.8. Mott–Schottky (MS) measurement

MS analysis is essential for the determination of the conduction band (CB) or valence band (VB) positions. The charge-transfer behavior can be predicted by the band positions between two phases in a semiconductor material. As ZNC-10G was a two-phase semiconductor based on the XRD pattern analysis, MS analysis could provide a hint of the flat-band positions, which are essential to determine the electron transfer between the phases in a semiconductor.⁸ In addition, the slope of the MS plot with $d(C^{-2})/dV$ provides the carrier density near the edge of the depletion region.⁷² Fig. 11 shows the MS spectra of the as-prepared ZNC-10G had two slopes, implying the formation of a heterojunction between the (Zn, Ni, Co)(O, S) and Ga_2O_3 phases. The similar slopes in the spectra revealed a comparable carrier density near the depletion zone with the n-type homojunction. As shown in the MS plot, the flat-band potentials of (Zn, Ni, Co)(O, S) and Ga_2O_3 were -0.20 and -0.70 V, respectively, indicating photogenerated electrons will transfer from the conduction bands of (Zn, Ni, Co)(O, S) to the oxygen vacancy states of Ga_2O_3 . As a result, the surface Ga_2O_3 will enhance the photocatalytic HER activity.

3.9. Photocatalytic activities of the HER

The catalytic activities of the ZNC-xG ($x = 0, 2.5, 5, 10$, and 20) catalysts were evaluated under the same experimental condition as mentioned in Section 2.4. Fig. 12a shows the photocatalytic HER with different Zn(O, S) systems to compare the

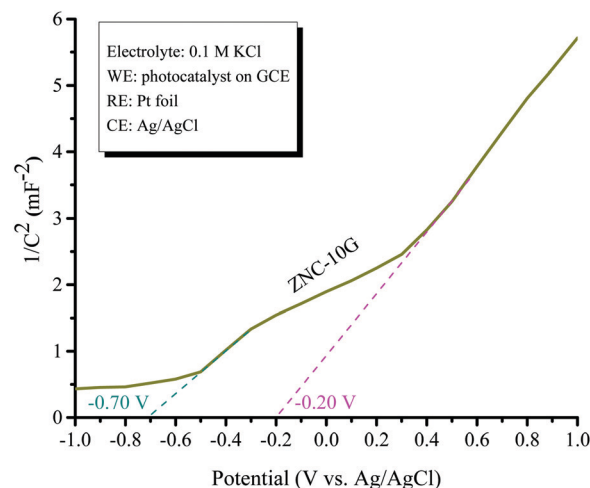


Fig. 11 Mott–Schottky plot of the as-prepared ZNC-10G catalyst in 0.1 M KCl electrolyte.

performances of the single dopants of Ni and Co with Ni–Co codopants systems. The synergistic effects of the Ni–Co codopants and the second phase of Ga_2O_3 were demonstrated. Fig. 12b shows the amounts of hydrogen production in the presence of different ZNC-xG catalysts with 10% ethanol as a hole scavenger agent. The results indicated that ZNC-xG ($x = 0, 2.5, 5, 10$, and 20) could generate 29.660, 30.630, 40.540, 44.570, and 27.930 $mmol\ g^{-1}\ h^{-1}$ H_2 gas, as confirmed by GC measurement. All the analyses results from DRS, PL, EIS, and TPC were consistent with the HER activities. The best optical and electrical properties were found in the ZNC-10G catalyst system, with the catalyst exhibiting the relevant properties with a higher light absorbance ability, lower photocarrier recombination process, lower charge-transfer resistivity, and higher transient photocurrent. The ZNC-0G catalyst with Ni and Co dopants also enhanced the HER by 36% compared to the pristine Zn(O, S).² After coupling with different Ga_2O_3 contents, ZNC-xG could enhance the HER activities. Although the wide-bandgap Ga_2O_3 does not contribute to the photoexcitation process, the existing oxygen vacancy states in Ga_2O_3 will help trapping photogenerated electrons from the CB of the (Zn, Ni, Co)(O, S) phase. As a result, a relatively high hydrogen evolution amount was shown for ZNC-10G. As shown in the ESI[†], the calculated apparent quantum yield (AQY) was $\sim 10.4\%$.

To highlight the performance of the present work, some recent works are listed as shown in Table 2 for comparison purposes. The performance of ZNC-10G was relatively high compared to the other systems without using noble metal, toxic sacrificial reagents, and a high-power lamp.

3.10. Photocatalytic hydrogen evolution mechanism

The HER activity of ZNC-xG ($x = 0, 2.5, 5, 10$, and 20) was induced by the photoexcitation of electrons and holes in the reduction and oxidation of water, respectively. The photocatalytic HER was initiated with a water oxidation reaction to provide protons and further reduced to form H_2 gas. When the ZNC-xG catalyst was illuminated by a 365 nm UV lamp with

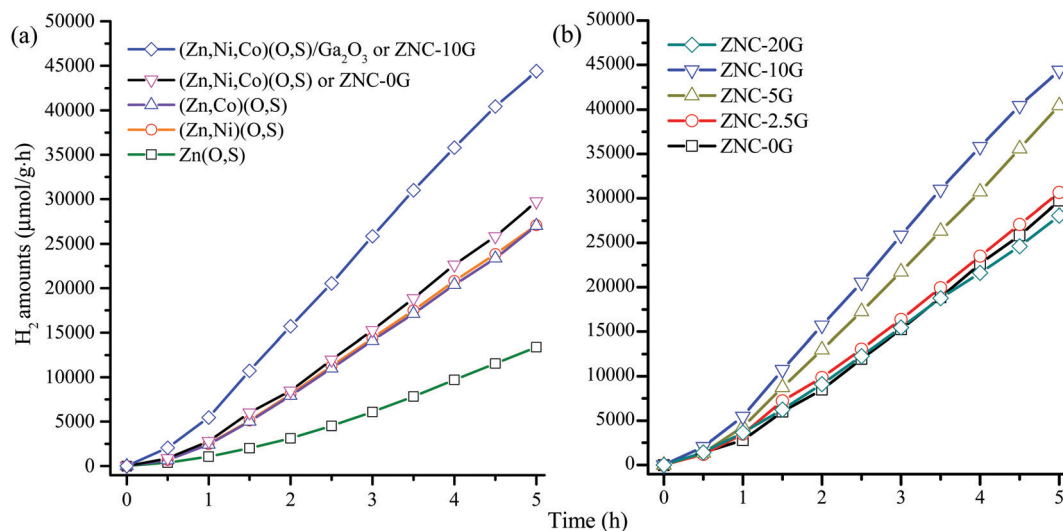


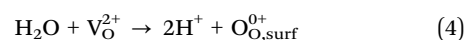
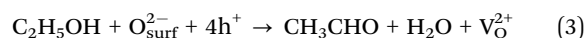
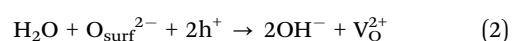
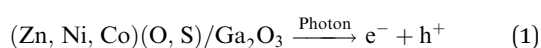
Fig. 12 Photocatalytic hydrogen evolution amounts in the presence of (a) different catalytic systems and (b) ZNC-xG catalysts with 10% ethanol as a hole scavenger in an aqueous solution.

Table 2 Other works with relatively high catalytic performances in the hydrogen evolution reaction for comparison

Catalysts	Cocatalyst	Light source	Sacrificial reagents	Hydrogen production rate ($\mu\text{mol g}^{-1} \text{h}^{-1}$)	Ref.
ZNC-10G	—	24 W UV tube lamp	10% V/V ethanol	9000	Present work
MoS ₂ /graphene	—	350 W Xe lamp	0.32 M formic acid	667	73
Ni-MOF-74/Ni ₂ P/MoS _x	Eosin Y	5 W White light	15% V/V triethanolamine	5723	74
NiP _x /MoS ₂ /NiS/CdS	MoS ₂ and NiP _x	Visible light	Glucose solution	297	75
NiS/ZnIn ₂ S ₄	—	320 W	50% lactic acid	250	76
TiO ₂	MoS _x	3 W LED, 365 nm	10% methanol	971	77
(Ni, In)(O, S) _{2-x}	—	250 W Xe lamp ($\lambda > 420 \text{ nm}$)	10% ethanol	305	78
MoS ₂ -NiS/CdS	—	300 W Xe lamp ($\lambda > 420 \text{ nm}$)	Lactic acid	25 252	79
Co(Ni)-doped MoS ₂	—	300 W Xe lamp	0.35 M Na ₂ SO ₃ /0.25 M Na ₂ S	20.9	80
MoS ₂ /Ti ₃ C ₂	Au	300 W Xe lamp	30% V/V methanol	12 000	81
MoS ₂	MoO ₂	300 W Xe lamp	0.4 M Na ₂ SO ₃ /0.4 M Na ₂ S	240	82

photon energy close to the bandgap energy of the as-prepared catalysts, the electron in VB is quickly excited to the CB. Different trapping states, such as Ni and Co dopants in Zn sites to form N_{Zn}^+ and CO_{Zn}^+ antisite defects in the Zn 4s4p orbitals, will help the charge separation.⁸³ Furthermore, the existence of an oxygen vacancy (V_{O}^{2+}) also will trap photogenerated electrons from recombination with holes.^{9,10,62} The oxygen vacancy sites possess a high energy adsorption for water.⁸⁴ Therefore, water molecules will attach to the oxygen vacancy sites to proceed with the oxidation reaction to generate H^+ . The photocatalytic HER is supported by photocarrier trapping with dopant-induced defects that lower the recombination rate and by water adsorption on the oxygen vacancy to enhance the oxidation reaction. In addition, the generated electron in the CB of (Zn, Ni, Co)(O, S) will transfer to the oxygen vacancy site in Ga_2O_3 for a further photocarrier separation.

The whole reaction mechanism can be written as follows:



Electrons and holes are generated as indicated in eqn (1) after light illumination. As indicated by the reversible change of the catalyst color from white to gray during the photocatalytic reaction, oxygen vacancy (V_{O}^{2+}) sites are formed on the catalyst surfaces. The formation of V_{O}^{2+} is initiated with water oxidation, as shown in eqn (2), involving Schottky defect oxygen anions and photogenerated holes. The further oxidation process proceeds as written in eqn (3) to oxidize ethanol to aldehyde with the formation of V_{O}^{2+} . Additional ethanol in the catalytic reaction will enhance the oxygen vacancy sites. Therefore, more diffused water on catalyst surfaces is trapped on the oxygen vacancy site and reduced to a proton during the reaction, as indicated in eqn (4).² The adsorbed proton on catalyst surfaces is finally reduced as released hydrogen gas in eqn (5). The reaction mechanism is schematically proposed in Fig. 13.

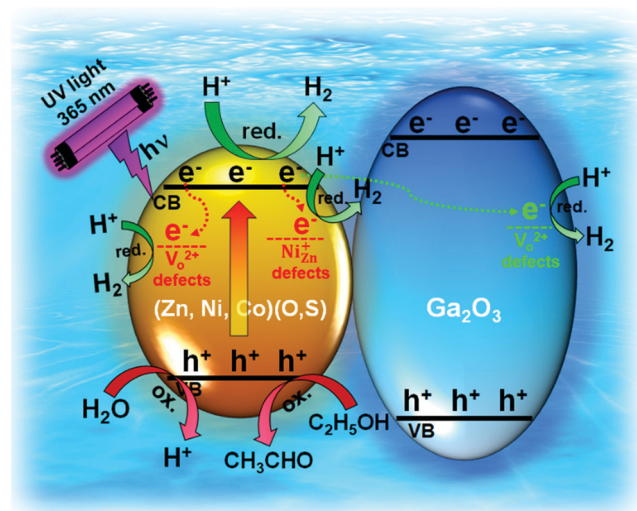


Fig. 13 Schematic photocatalytic HER reaction mechanism in the presence of ZNC-10G in 10% ethanol solution as a hole scavenger under blacklight 365 nm UV tube lamp illumination.

Table 3 BET analysis results of ZNC-0G and ZNC-10G

Catalysts	Precursors (mmol)					BET results		
	Zn	Ni	Co	Ga	TAA	Surface area (m ² g ⁻¹)	Pore size (nm)	Pore volume (m ³ g ⁻¹)
ZNC-0G	20	10	0.5	—	10	43.916	18.618	0.204
ZNC-10G	20	10	0.5	2	10	64.27	21.284	0.342

Enhanced catalytic activities with the Ni³⁺ dopant have also been observed in some previous works to increase the optical absorbance of the catalyst^{85,86} and to provide oxygen vacancy sites for weak electrostatic binding. As a result, the electron in the Vo is delocalized and the Ni³⁺ ion induces a facile electron transfer from the Vo to Ni sites to enhance the conductivity.⁸⁵ In addition, The underlying chemistries include the near-unity occupancy of the e_g orbital (t_{2g}⁶-e_g¹) of Ni³⁺, which speeds up the electron transfer and significantly promotes the excellent electron-hole separation efficiency, and establishes the outstanding overall charge-transfer efficiency and long-term photocatalytic activity.⁸⁶ The role of the Co dopant is also supported by previous works; whereby it can suppress charge recombination and improve the catalytic activities,⁸⁷ enhance the stability and recyclability of a catalytic system,⁸⁸ and improve the hydrogen production and hydrogenation reaction.¹⁰ In addition, DFT calculations have also revealed that Co-doping reduces the H binding free energy for the HER.⁸⁹

Furthermore, the catalytic activities were also supported by the BET analysis, which was performed to probe the surface area, pore size, and pore volume, as shown in Table 3. The surface area, pore size, and pore volume of ZNC-0G were lower than those of ZNC-10G, indicating there were more active sites on ZNC-10G to catalytically evolve hydrogen gas during the photoreaction. The characteristic N₂ adsorption-desorption curves and pore-size distribution are also shown in Fig. 14.

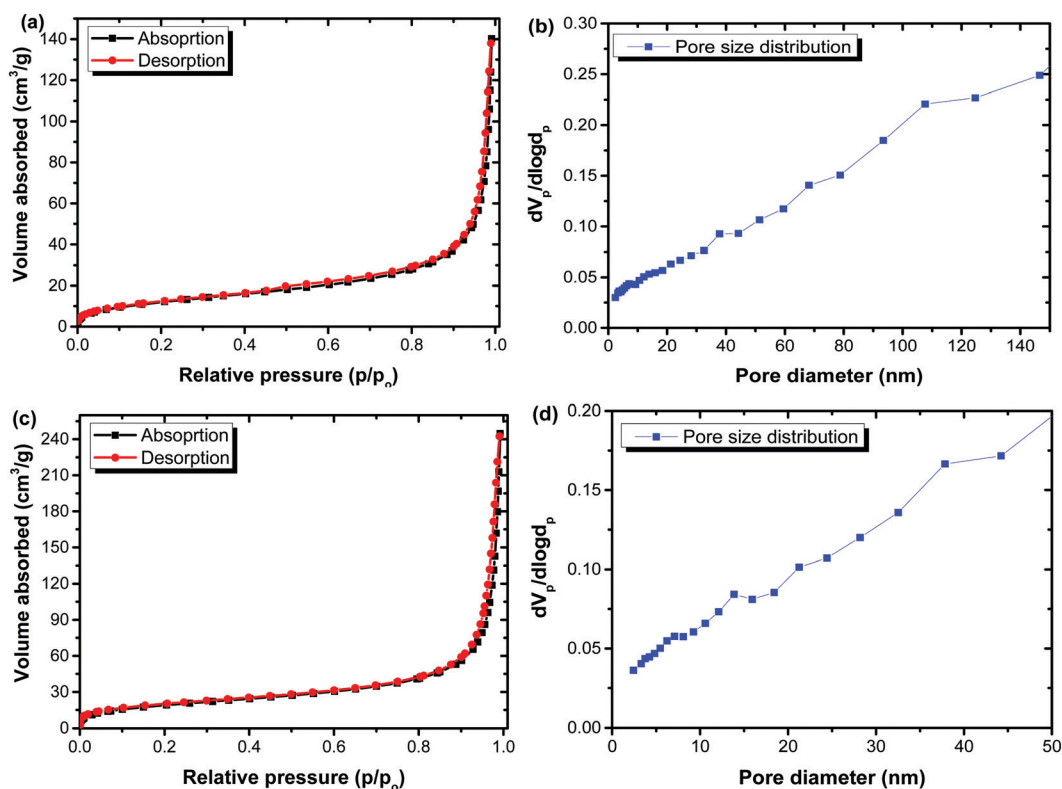


Fig. 14 (a and c) Nitrogen adsorption-desorption curves and (b and d) pore-size distribution of (a and b) ZNC-0G and (c and d) ZNC-10G.

4. Conclusions

Multicomponent (Zn, Ni, Co)(O, S)/Ga₂O₃ nanocomposites with different Ga₂O₃ contents were successfully synthesized, characterized, and tested toward the photocatalytic HER. The results of XRD, SEM, and TEM analyses confirmed the phases in the nanocomposites. XPS analysis indicated the formation of oxygen vacancy sites on the nanocomposites, which played an essential role in oxidizing water and enhancing water adsorption. Co²⁺, Ni²⁺ and Ni³⁺ were also found in the XPS analysis and they contributed to Co_{Zn}⁰⁺, Ni_{Zn}⁰⁺, and Ni_{Zn}⁺ antisite defects formation, which support trapping photogenerated electrons, leading to a high HER catalytic performance. In addition, the role of Ga₂O₃ was to provide oxygen vacancy states to trap electrons from the CB of (Zn, Ni, Co)(O, S), suggesting a better separation of photocarriers after photoexcitation. As a result, ZNC-10G with the optimized amount of Ga₂O₃ could evolve ~9 mmol g⁻¹ h under low-power UV light illumination. The strategy with Ni-Co dopants and nanocomposite formation to enhance hydrogen production was demonstrated to be effective and shows potential as part of a solution for replacing carbon-based fossil fuels in the future.

Conflicts of interest

There are no conflicts to declare.

Acknowledgements

This work is supported by the ministry of research and technology of Indonesia with a scheme of Penelitian Terapan Unggulan Perguruan Tinggi (PTUPT) funding received by Dr Hairus Abdullah, based on the research contract between regional higher education service institutions I (LLDIKTI-I) and Universitas Prima Indonesia with a grant number of 317/LL1/PG/2021 dated 16th July 2021.

References

- 1 H. Abdullah, N. S. Gultom and D.-H. Kuo, A simple one-pot synthesis of Zn(O, S)/Ga₂O₃ nanocomposite photocatalyst for hydrogen production and 4-nitrophenol reduction, *New J. Chem.*, 2017, **41**, 12397–12406.
- 2 H. Abdullah, D.-H. Kuo and X. Chen, High efficient noble metal free Zn(O, S) nanoparticles for hydrogen evolution, *Int. J. Hydrogen Energy*, 2017, **42**(9), 5638–5648.
- 3 X. Huang, L. Yang, S. Hao, B. Zheng, L. Yan, F. Qu, A. M. Asiri and X. Sun, N-Doped carbon dots: a metal-free co-catalyst on hematite nanorod arrays toward efficient photoelectrochemical water oxidation, *Inorg. Chem. Front.*, 2017, **4**(3), 537–540.
- 4 C. Marchal, A. Piquet, M. Behr, T. Cottineau, V. Papaefthimiou, V. Keller and V. Caps, Activation of solid grinding-derived Au/TiO₂ photocatalysts for solar H₂ production from water-methanol mixtures with low alcohol content, *J. Catal.*, 2017, **352**, 22–34.
- 5 S. Nanda, R. Rana, Y. Zheng, J. A. Kozinski and A. K. Dalai, Insights on pathways for hydrogen generation from ethanol, *Sustainable Energy Fuels*, 2017, **1**, 1232–1245.
- 6 M. Ye, X. Gao, X. Hong, Q. Liu, C. He, X. Liu and C. Lin, Recent advances in quantum dot-sensitized solar cells: insights into photoanodes, sensitizers, electrolytes and counter electrodes, *Sustainable Energy Fuels*, 2017, **1**, 1217–1231.
- 7 H. Abdullah, N. S. Gultom, D.-H. Kuo and A. D. Saragih, Cobalt-doped Zn(O, S)/Ga₂O₃ nanoheterojunction composites for enhanced hydrogen production, *New J. Chem.*, 2018, **42**, 9626–9634.
- 8 H. Abdullah, N. S. Gultom and D.-H. Kuo, Depletion-Zone size control of p-type NiO/n-type Zn(O, S) nanodiodes on high-surface-area SiO₂ nanoparticles as a strategy to significantly enhance hydrogen evolution rate, *Appl. Catal., B*, 2020, **261**, 118223.
- 9 H. Shuwanto, H. Abdullah, D.-H. Kuo and N. S. Gultom, Surface active sites of Y-doped Zn(O, S) for chemisorption and hydrogenation of azobenzene and nitroaromatic compounds under light via self-generated proton, *Appl. Surf. Sci.*, 2021, **552**, 149508.
- 10 H. Shuwanto, N. S. Gultom, H. Abdullah and D.-H. Kuo, Environmentally Benign Photoreactions for Hydrogen Production and Cleavage of N=N bond in Azobenzene over Co-Doped Zn(O, S) Nanocatalyst: The Role of In Situ Generated H⁺, *ACS Appl. Energy Mater.*, 2020, **3**(12), 12692–12702.
- 11 O. A. Zelekew, D.-H. Kuo and H. Abdullah, Synthesis of (Sn, Zn)(O, S) bimetallic oxysulfide catalyst for the detoxification of Cr⁶⁺ in aqueous solution, *Adv. Powder Technol.*, 2019, **30**(12), 3099–3106.
- 12 L. Yuliati, M. Kimi and M. Shamsuddin, High activity of Ag-doped Cd_{0.1}Zn_{0.9}S photocatalyst prepared by the hydrothermal method for hydrogen production under visible-light irradiation, *Beilstein J. Nanotechnol.*, 2014, **5**, 587–595.
- 13 T. Bai, X. Shi, M. Liu, H. Huang, M.-H. Yu, J. Zhang and X.-H. Bu, Metal-organic Framework-derived Zn_{1-x}Cd_xS/CdS Heterojunction for Efficient Visible Light-driven Photocatalytic Hydrogen Production, *Dalton Trans.*, 2021, **50**, 6064–6070.
- 14 X. Lu, J. Xie, X. Chen and X. Li, Engineering MP_x (M = Fe, Co or Ni) interface electron transfer channels for boosting photocatalytic H₂ evolution over g-C₃N₄/MoS₂ layered heterojunctions, *Appl. Catal., B*, 2019, **252**, 250–259.
- 15 N. Xiao, S. Li, S. Liu, B. Xu, Y. Li, Y. Gao, L. Ge and G. Lu, Novel PtPd alloy nanoparticle-decorated g-C₃N₄ nanosheets with enhanced photocatalytic activity for H₂ evolution under visible light irradiation, *Chin. J. Catal.*, 2019, **40**(3), 352–361.
- 16 A. M. Elewa, A. F. M. El-Mahdy, M. H. Elsayed, M. G. Mohamed, S.-W. Kuo and H.-H. Chou, Sulfur-doped Triazine-Conjugated Microporous Polymers for Achieving the Robust Visible-light-driven Hydrogen Evolution, *Chem. Eng. J.*, 2021, 129825.
- 17 D. Van Dao, H. D. Jung, T. T. D. Nguyen, S.-W. Ki, H. Son, K.-B. Bae, T. D. Le, Y.-H. Cho, J.-K. Yang, Y.-T. Yu, S. Back

- and I.-H. Lee, Defect-rich N-doped CeO₂ supported by N-doped graphene as a metal-free plasmonic hydrogen evolution photocatalyst, *J. Mater. Chem. A*, 2021, **9**, 10217–10230.
- 18 Z. Chang, L. Zhu, J. Zhao, P. Chen, D. Chen and H. Gao, NiMo/Cu-nanosheets/Ni-foam composite as a high performance electrocatalyst for hydrogen evolution over a wide pH range, *Int. J. Hydrogen Energy*, 2020, **46**(5), 3493–3503.
 - 19 N. Gurbani, N. Chouhan, R. J. Choudhary, D. M. Phase, K. Marumoto and R.-S. Liu, Graphene Oxide @ Nickel Phosphate Nanocomposites for Photocatalytic Hydrogen Production, *Adv. Chem. Eng.*, 2021, 100105.
 - 20 Y. Li, Z. Jin, L. Zhang and K. Fan, Controllable design of Zn-Ni-P on g-C₃N₄ for efficient photocatalytic hydrogen production, *Chin. J. Catal.*, 2019, **40**(3), 390–402.
 - 21 Z. Li, Y. Ma, X. Hu, E. Liu and J. Fan, Enhanced photocatalytic H₂ production over dual-cocatalyst-modified g-C₃N₄ heterojunctions, *Chin. J. Catal.*, 2019, **40**(3), 434–445.
 - 22 Y. Ren, D. Zeng and W.-J. Ong, Interfacial engineering of graphitic carbon nitride (g-C₃N₄)-based metal sulfide heterojunction photocatalysts for energy conversion: A review, *Chin. J. Catal.*, 2019, **40**(3), 289–319.
 - 23 D. Ren, W. Zhang, Y. Ding, R. Shen, Z. Jiang, X. Lu and X. Li, In Situ Fabrication of Robust Cocatalyst-Free CdS/g-C₃N₄ 2D–2D Step-Scheme Heterojunctions for Highly Active H₂ Evolution, *Sol. RRL*, 2020, **4**(8), 1900423.
 - 24 H. Xu, R. Xiao, J. Huang, Y. Jiang, C. Zhao and X. Yang, In situ construction of protonated g-C₃N₄/Ti₃C₂ MXene Schottky heterojunctions for efficient photocatalytic hydrogen production, *Chin. J. Catal.*, 2021, **42**(1), 107–114.
 - 25 L. Hu, H. Yang, S. Wang, J. Gao, H. Hou and W. Yang, MOF-derived Hexagonal In₂O₃ Microrods Decorated with g-C₃N₄ Ultrathin Nanosheets for Efficient Photocatalytic Hydrogen Production, *J. Mater. Chem. C*, 2021, **9**, 5343–5348.
 - 26 J. Cai, A. Cao, J. Huang, W. Jin, J. Zhang, Z. Jiang and X. Li, Understanding oxygen vacancies in disorder-engineered surface and subsurface of CaTiO₃ nanosheets on photocatalytic hydrogen evolution, *Appl. Catal., B*, 2020, **267**, 118378.
 - 27 R. K. Chava, N. Son and M. Kang, Fabrication of oxygen vacancy rich ultrafine ceria nanocubes decorated one dimensional CdS heteronanostructures for efficient visible light driven hydrogen evolution reaction, *Appl. Surf. Sci.*, 2021, **556**, 149731.
 - 28 C. Chen, G. Qiu, T. Wang, Z. Zheng, M. Huang and B. Li, Modulating oxygen vacancies on bismuth-molybdate hierarchical hollow microspheres for photocatalytic selective alcohol oxidation with hydrogen peroxide production, *J. Colloid Interface Sci.*, 2021, **592**, 1–12.
 - 29 F. T. Bakena, H. Abdullah, D.-H. Kuo and M. A. Zeleke, Photocatalytic reduction of 4-nitrophenol using effective hole scavenger over novel Mg-doped Zn(O, S) nanoparticles, *J. Ind. Eng. Chem.*, 2019, **78**, 116–124.
 - 30 S. Iguchi, K. Teramura, S. Hosokawa and T. Tanaka, Effect of the chloride ion as a hole scavenger on the photocatalytic conversion of CO₂ in an aqueous solution over Ni–Al layered double hydroxides, *Phys. Chem. Chem. Phys.*, 2015, **17**(27), 17995–18003.
 - 31 G. Yang, Q. Chen, W. Wang, S. Wu, B. Gao, Y. Xu, Z. Chen, S. Zhong, J. Chen and S. Bai, Cocatalyst Engineering in Piezocatalysis: A Promising Strategy for Boosting Hydrogen Evolution, *ACS Appl. Mater. Interfaces*, 2021, **13**(13), 15305–15314.
 - 32 R. Shen, J. Xie, Q. Xiang, X. Chen, J. Jiang and X. Li, Ni-based photocatalytic H₂-production cocatalysts, *Chin. J. Catal.*, 2019, **40**(3), 240–288.
 - 33 J. Pan, S. Shen, W. Zhou, J. Tang, H. Ding, J. Wang, L. Chen, C. T. Au and S. F. Yin, Recent Progress in Photocatalytic Hydrogen Evolution, *Acta Phys. – Chim. Sin.*, 2020, **36**(3), 1905068.
 - 34 Z. Liang, R. Shen, Y. H. Ng, P. Zhang, Q. Xiang and S. Li, A review on 2D MoS₂ cocatalysts in photocatalytic H₂ production, *J. Mater. Sci. Technol.*, 2020, **56**, 89–121.
 - 35 F. Tong, X. Liang, F. Ma, X. Bao, Z. Wang, Y. Liu, P. Wang, H. Cheng, Y. Dai, B. Huang and Z. Zheng, Plasmon-Mediated Nitrobenzene Hydrogenation with Formate as the Hydrogen Donor Studied at a Single-Particle Level, *ACS Catal.*, 2021, 3801–3809.
 - 36 S. Wang, H. Sun, P. Qiao, Z. Li, Y. Xie and W. Zhou, NiS/Pt nanoparticles co-decorated black mesoporous TiO₂ hollow nanotube assemblies as efficient hydrogen evolution photocatalysts, *Appl. Mater. Today*, 2021, **22**, 100977.
 - 37 H. Abdullah and D.-H. Kuo, Photocatalytic Performance of Ag and CuBiS₂ Nanoparticle-Coated SiO₂@TiO₂ Composite Sphere under Visible and Ultraviolet Light Irradiation for Azo Dye Degradation with the Assistance of Numerous Nano p–n Diodes, *J. Phys. Chem. C*, 2015, **119**(24), 13632–13641.
 - 38 D.-H. Kuo, H. Abdullah, N. S. Gultom and J.-Y. Hu, Ag-Decorated MoS_x Laminar-Film Electrocatalyst Made with Simple and Scalable Magnetron Sputtering Technique for Hydrogen Evolution: A Defect Model to Explain the Enhanced Electron Transport, *ACS Appl. Mater. Interfaces*, 2020, **12**(31), 35011–35021.
 - 39 N. R. Reddy, U. Bharagav, M. V. Shankar, P. M. Reddy, K. R. Reddy, N. P. Shetti, F. Alonso-Marroquin, M. M. Kumari, T. M. Aminabhavi and S. W. Joo, Photocatalytic hydrogen production by ternary heterojunction composites of silver nanoparticles doped FCNT-TiO₂, *J. Environ. Manage.*, 2021, **286**, 112130.
 - 40 H. Abdullah, R. Siburian, S. P. Pasaribu and A. S. Panggabean, Visible-Light Driven Ni-Incorporated CdS Photocatalytic Activities for Azo-Bond Cleavages with Hydrogenation Reaction, *ChemistrySelect*, 2021, **6**(9), 2041–2050.
 - 41 A. Walsh, J. L. F. Da Silva and S.-H. Wei, Multi-component transparent conducting oxides: progress in materials modelling, *J. Phys.: Condens. Matter*, 2011, **23**(33), 334210.
 - 42 C.-J. Chang, J.-K. Chen, K.-S. Lin, C.-Y. Huang and C.-L. Huang, Improved H₂ production of ZnO@ZnS nanorod-decorated Ni foam immobilized photocatalysts, *Int. J. Hydrogen Energy*, 2020, **46**(20), 11357–11368.
 - 43 V. N. Rao, P. Ravi, M. Sathish, N. L. Reddy, K. Lee, M. Sakar, P. Prathap, M. M. Kumari, K. R. Reddy, M. N. Nadagouda, T. M. Aminabhavi and M. V. Shankar, Monodispersed core/shell nanospheres of ZnS/NiO with enhanced H₂ generation

- and quantum efficiency at versatile photocatalytic conditions, *J. Hazard. Mater.*, 2021, 125359.
- 44 W. Zhao, T. She, J. Zhang, G. Wang, S. Zhang, W. Wei, G. Yang, L. Zhang, D. Xia, Z. Cheng, H. Huang and D. Y. C. Leung, A novel Z-scheme $\text{CeO}_2/\text{g-C}_3\text{N}_4$ heterojunction photocatalyst for degradation of Bisphenol A and hydrogen evolution and insight of the photocatalysis mechanism, *J. Mater. Sci. Technol.*, 2021, **85**, 18–29.
 - 45 X. Zhang, Z. Cheng, P. Deng, L. Zhang and Y. Hou, $\text{NiSe}_2/\text{Cd}_{0.5}\text{Zn}_{0.5}\text{S}$ as a type-II heterojunction photocatalyst for enhanced photocatalytic hydrogen evolution, *Int. J. Hydrogen Energy*, 2021, **46**(29), 15389–15397.
 - 46 M. Yang, K. Wang, Y. Li, K. Yang and Z. Jin, Pristine hexagonal CdS assembled with NiV LDH nanosheet formed p-n heterojunction for efficient photocatalytic hydrogen evolution, *Appl. Surf. Sci.*, 2021, **548**, 149212.
 - 47 L. Xu, J. Zeng, Q. Li, L. Xia, X. Luo, Z. Ma, B. Peng, S. X. Xiong, Z. Li, L.-L. Wang and Y. Lei, Defect-engineered 2D/2D hBN/g- C_3N_4 Z-scheme heterojunctions with full visible-light absorption: Efficient metal-free photocatalysts for hydrogen evolution, *Appl. Surf. Sci.*, 2021, **547**, 149207.
 - 48 I.-H. Lee, D. V. Dao, T. T. D. Nguyen, S. Hoki, H. D. Jung, S. Back, S.-W. Ki, K.-B. Bae, T. D. Le, Y.-H. Cho, J.-K. Yang and Y.-T. Yu, Defect-rich N-doped CeO_2 supported by N-doped graphene as a metal-free plasmonic hydrogen evolution photocatalyst, *J. Mater. Chem. A*, 2021, **9**, 10217–10230.
 - 49 A. Yamakata, J. J. M. Vequizo, T. Ogawa, K. Kato, S. Tsuboi, N. Furutani, M. Ohtsuka, S. Muto, A. Kuwabara and Y. Sakata, Core-Shell Double Doping of Zn and Ca on $\beta\text{-Ga}_2\text{O}_3$ Photocatalysts for Remarkable Water Splitting, *ACS Catal.*, 2021, **11**(4), 1911–1919.
 - 50 Y. Liu, L. Ma, C. Shen, X. Wang, X. Zhou, Z. Zhao and A. Xu, Highly enhanced visible-light photocatalytic hydrogen evolution on g- C_3N_4 decorated with vopce through π - π interaction, *Chin. J. Catal.*, 2019, **40**(2), 168–176.
 - 51 J. D. Juanjuan Huang, H. Du, G. Xu and Y. Yuan, Control of Nitrogen Vacancy in g- C_3N_4 by Heat Treatment in an Ammonia Atmosphere for Enhanced Photocatalytic Hydrogen Generation, *Acta Phys. – Chim. Sin.*, 2020, **36**(7), 1905056.
 - 52 N. S. Gultom, H. Abdullah and D.-H. Kuo, Enhanced photocatalytic hydrogen production of noble-metal free Ni-doped Zn(O, S) in ethanol solution, *Int. J. Hydrogen Energy*, 2017, **42**(41), 25891–25902.
 - 53 H. She, Y. Sun, S. Li, J. Huang, L. Wang, G. Zhu and Q. Wang, Synthesis of non-noble metal nickel doped sulfide solid solution for improved photocatalytic performance, *Appl. Catal., B*, 2019, **245**, 439–447.
 - 54 Z. Bai, S. Li, J. Fu, Q. Zhang, F. Chang, L. Yang, J. Lu and Z. Chen, Metal-organic framework-derived Nickel Cobalt oxy-sulfide nanocages as trifunctional electrocatalysts for high efficiency power to hydrogen, *Nano Energy*, 2019, **58**, 680–686.
 - 55 H. Wan, L. Li, J. Zhang, X. Liu, H. Wang and H. Wang, Nickel Nanowire@Porous NiCo_2O_4 Nanorods Arrays Grown on Nickel Foam as Efficient Pseudocapacitor Electrode, *Front. Energy Res.*, 2017, **5**(33), 1–7.
 - 56 Z. Ye, L. Qiu, W. Yang, Z. Wu, Y. Liu, G. Wang, Y. Song, B. Zhong and X. Guo, Recent progress of Nickel-rich layered cathode materials for lithium ion batteries, *Chem. – Eur. J.*, 2021, **27**, 4249–4269.
 - 57 J. Langdon and A. Manthiram, Crossover Effects in Batteries with High-Nickel Cathodes and Lithium-Metal Anodes, *Adv. Funct. Mater.*, 2021, **31**(17), 2010267.
 - 58 S. Iguchi, Y. Hasegawa, K. Teramura, S. Kidera, S. Kikkawa, S. Hosokawa, H. Asakura and T. Tanaka, Drastic improvement in the photocatalytic activity of Ga_2O_3 modified with Mg-Al layered double hydroxide for the conversion of CO_2 in water, *Sustainable Energy Fuels*, 2017, **1**, 1740–1747.
 - 59 H. Abdullah and D.-H. Kuo, Facile Synthesis of n-type $(\text{AgIn})_x\text{Zn}_{2(1-x)}\text{S}_2$ /p-type Ag_2S Nanocomposite for Visible Light Photocatalytic Reduction To Detoxify Hexavalent Chromium, *ACS Appl. Mater. Interfaces*, 2015, **7**(48), 26941–26951.
 - 60 H. Abdullah, N. S. Gultom and D.-H. Kuo, A simple one-pot synthesis of a Zn(O, S)/ Ga_2O_3 nanocomposite photocatalyst for hydrogen production and 4-nitrophenol reduction, *New J. Chem.*, 2017, **41**(21), 12397–12406.
 - 61 N. S. Gultom, H. Abdullah and D.-H. Kuo, Facile synthesis of cobalt-doped $(\text{Zn, Ni})(\text{O, S})$ as an efficient photocatalyst for hydrogen production, *J. Energy Inst.*, 2018, **92**(5), 1428–1439.
 - 62 H. Abdullah, N. S. Gultom, H. Shuwanto, W. L. Kebede and D.-H. Kuo, Self-Protonated Ho-Doped Zn(O, S) as a Green Chemical-Conversion Catalyst to Hydrogenate Nitro to Amino Compounds, *ACS Appl. Mater. Interfaces*, 2020, **12**(39), 43761–43770.
 - 63 H. Abdullah, D. H. Kuo and X. Y. Chen, High efficient noble metal free Zn(O, S) nanoparticles for hydrogen evolution, *Int. J. Hydrogen Energy*, 2017, **42**(9), 5638–5648.
 - 64 J. C. Slater, Atomic Radii in Crystals, *J. Chem. Phys.*, 1964, **41**(10), 3199–3204.
 - 65 M. Saleh, K. G. Lynn, L. G. Jacobsohn and J. S. McCloy, Luminescence of undoped commercial ZnS crystals: A critical review and new evidence on the role of impurities using photoluminescence and electrical transient spectroscopy, *J. Appl. Phys.*, 2019, **125**(7), 075702.
 - 66 V. Mihalache, C. Negriila, V. Bercu, M. Secu, E. Vasile and G. E. Stan, Effect of dilute doping and non-equilibrium synthesis on the structural, luminescent and magnetic properties of nanocrystalline $\text{Zn}_{1-x}\text{Ni}_x\text{O}$ ($x = 0.0025\text{--}0.03$), *Mater. Res. Bull.*, 2019, **115**, 37–48.
 - 67 D. Xiong, W. Li and L. Liu, Vertically Aligned Porous Nickel(II) Hydroxide Nanosheets Supported on Carbon Paper with Long-Term Oxygen Evolution Performance, *Chem. – Asian J.*, 2017, **12**(5), 543–551.
 - 68 A. Khorsand Zak, N. S. Abd Aziz, A. M. Hashim and F. Kordi, XPS and UV-vis studies of Ga-doped zinc oxide nanoparticles synthesized by gelatin based sol-gel approach, *Ceram. Int.*, 2016, **42**(12), 13605–13611.
 - 69 H. Abdullah, C.-N. Hsu, H. Shuwanto, N. S. Gultom, W. L. Kebede, C.-M. Wu, C.-C. Lai, R.-I. Murakami, M. Hirota, A. N. Nakagaito and D.-H. Kuo, Immobilization of cross-linked in-doped $\text{Mo}(\text{O, S})_2$ on cellulose nanofiber for effective organic-compound degradation under visible

- light illumination, *Prog. Nat. Sci.: Mater. Int.*, 2021, **31**(3), 404–413.
- 70 X. Chen, H. Abdullah and D.-H. Kuo, CuMnOS Nanoflowers with Different $\text{Cu}^+/\text{Cu}^{2+}$ Ratios for the CO_2 -to- CH_3OH and the CH_3OH -to- H_2 Redox Reactions, *Sci. Rep.*, 2017, **7**, 41194.
 - 71 C. L. C. Ellis; E. Smith; H. Javadi; G. Berns and D. Venkataraman, Ion Migration in Hybrid Perovskites: Evolving Understanding of a Dynamic Phenomenon, in *Perovskite Photovoltaics*, ed. S. Thomas and A. Thankappan, Academic Press: 2018, ch. 6, pp. 163–196.
 - 72 B. Klahr, S. Gimenez, F. Fabregat-Santiago, T. Hamann and J. Bisquert, Water Oxidation at Hematite Photoelectrodes: The Role of Surface States, *J. Am. Chem. Soc.*, 2012, **134**(9), 4294–4302.
 - 73 G.-J. Lee, Y.-H. Hou, C.-Y. Chen, C.-Y. Tsay, Y.-C. Chang, J.-H. Chen, T.-L. Horng, S. Anandan and J. J. Wu, Enhanced performance for photocatalytic hydrogen evolution using MoS_2 /graphene hybrids, *Int. J. Hydrogen Energy*, 2021, **46**(8), 5938–5948.
 - 74 T. Li and Z. Jin, Unique ternary Ni-MOF-74/ $\text{Ni}_2\text{P}/\text{MoS}_x$ composite for efficient photocatalytic hydrogen production: Role of Ni_2P for accelerating separation of photogenerated carriers, *J. Colloid Interface Sci.*, 2022, **605**, 385–397.
 - 75 X. Zheng, X. Wang, J. Liu, X. Fu, Y. Yang, H. Han, Y. Fan, S. Zhang, S. Meng and S. Chen, Construction of $\text{NiP}_x/\text{MoS}_2/\text{NiS}/\text{CdS}$ composite to promote photocatalytic H_2 production from glucose solution, *J. Am. Ceram. Soc.*, 2021, **104**(10), 5307–5316.
 - 76 A. Yan, X. Shi, F. Huang, M. Fujitsuka and T. Majima, Efficient photocatalytic H_2 evolution using $\text{NiS}/\text{ZnIn}_2\text{S}_4$ heterostructures with enhanced charge separation and interfacial charge transfer, *Appl. Catal., B*, 2019, **250**, 163–170.
 - 77 J. He, W. Zhong, Y. Xu, J. Fan, H. Yu and J. Yu, Highly dispersed MoS_x nanodot-modified TiO_2 photocatalysts: vitamin C-mediated synthesis and improved H_2 evolution activity, *J. Mater. Chem. C*, 2021, **9**(9), 3239–3246.
 - 78 X. Chen, T. Huang, D.-H. Kuo, H. Sun, P. Li, O. A. Zelekew, A. B. Abdeta, Q. Wu, J. Zhang, Z. Yuan and J. Lin, Material design with the concept of solid solution-type defect engineering in realizing the conversion of an electrocatalyst of NiS_2 into a photocatalyst for hydrogen evolution, *Appl. Catal., B*, 2021, **298**, 120542.
 - 79 M. Yin, W. Zhang, F. Qiao, J. Sun, Y. Fan and Z. Li, Hydrothermal synthesis of MoS_2 - NiS/CdS with enhanced photocatalytic hydrogen production activity and stability, *J. Solid State Chem.*, 2019, **270**, 531–538.
 - 80 X. Ma, J. Li, C. An, J. Feng, Y. Chi, J. Liu, J. Zhang and Y. Sun, Ultrathin Co(Ni)-doped MoS_2 nanosheets as catalytic promoters enabling efficient solar hydrogen production, *Nano Res.*, 2016, **9**(8), 2284–2293.
 - 81 J. Zhang, M. Liu, Y. Wang and F. Shi, Au/ $\text{MoS}_2/\text{Ti}_3\text{C}_2$ composite catalyst for efficient photocatalytic hydrogen evolution, *CrystEngComm*, 2020, **22**(21), 3683–3691.
 - 82 Y. Zhang, S. Guo, X. Xin, Y. Song, L. Yang, B. Wang, L. Tan and X. Li, Plasmonic MoO_2 as co-catalyst of MoS_2 for enhanced photocatalytic hydrogen evolution, *Appl. Surf. Sci.*, 2020, **504**, 144291.
 - 83 M. Dong, J. Zhang and J. Yu, Effect of effective mass and spontaneous polarization on photocatalytic activity of wurtzite and zinc blende ZnS , *APL Mater.*, 2015, **3**(10), 104404.
 - 84 H. Heydari, M. Elahifard and R. Behjatmanesh-Ardakani, Role of oxygen vacancy in the adsorption and dissociation of the water molecule on the surfaces of pure and Ni-doped rutile (110): a periodic full-potential DFT study, *Surf. Sci.*, 2019, **679**, 218–224.
 - 85 J. Chen, G.-H. Lu, H. Cao, T. Wang and Y. Xu, Ferromagnetic mechanism in Ni-doped anatase TiO_2 , *Appl. Phys. Lett.*, 2008, **93**(17), 172504.
 - 86 K. Raju, S. Rajendran, T. K. A. Hoang, D. Durgalakshmi, J. Qin, D. E. Diaz-Droguett, F. Gracia and M. A. Gracia-Pinilla, Photosynthesis of H_2 and its storage on the Bandgap Engineered Mesoporous $(\text{Ni}^{2+}/\text{Ni}^{3+})\text{O}@\text{TiO}_2$ heterostructure, *J. Power Sources*, 2020, **466**, 228305.
 - 87 Y. Zheng, J. Dong, C. Huang, L. Xia, Q. Wu, Q. Xu and W. Yao, Co-doped Mo-Mo $_2\text{C}$ cocatalyst for enhanced g- C_3N_4 photocatalytic H_2 evolution, *Appl. Catal., B*, 2020, **260**, 118220.
 - 88 E.-C. Cho, C.-W. Chang-Jian, J.-H. Huang, G.-Y. Lee, W.-H. Hung, M.-Y. Sung, K.-C. Lee, H. C. Weng, W.-L. Syu, Y.-S. Hsiao and C.-P. Chen, Co^{2+} -Doped $\text{BiOBr}_x\text{Cl}_{1-x}$ hierarchical microspheres display enhanced visible-light photocatalytic performance in the degradation of rhodamine B and antibiotics and the inactivation of *E. coli*, *J. Hazard. Mater.*, 2021, **402**, 123457.
 - 89 Z. Liang, Y. Xue, X. Wang, Y. Zhou, X. Zhang, H. Cui, G. Cheng and J. Tian, Co doped MoS_2 as cocatalyst considerably improved photocatalytic hydrogen evolution of g- C_3N_4 in an alkaline environment, *Chem. Eng. J.*, 2021, **421**, 130016.